V International Conference on Simulation for Additive Manufacturing
Sim-AM 2025
F. Auricchio, M. Carraturo and S. Morganti (Eds)

ANALYSIS ON SPATTER BEHAVIOUR IN POWDER BED FUSION USING SOLID-GAS MULTIPHASE ANALYSIS

Y. NAKAMURA[*], R. KOIKE[*], Y. KAKINUMA[*], Y. HIRONO[†], T. MORI[†] AND K. YAMAZAKI[†]

[*] Department of System Design Engineering, Faculty of Science & Technology, Keio University
3-14-1 Hiyoshi, Kohoku-ku, Yokohama, Japan
e-mail: yusuke5011@keio.jp, web page: http://koikelab.sd.keio.ac.jp/main/

[†] DMG MORI CO., LTD.
2-3-23 Shiomi, Koto-ku, Tokyo, Japan
web page: https://www.dmgmori.co.jp/

Key words: Additive manufacturing (AM), Powder bed fusion (PBF), Computational fluid dynamics (CFD), Discrete phase model (DPM), Spatter, Fume

Abstract. *Powder Bed Fusion (PBF), one of metal additive manufacturing processes comparably has high fabrication resolution, resulting in spread of its applications in aviation and automotive industries. However, the adherence of spatter to the build surface deteriorates the fabrication quality and fume induces laser attenuation and shifts the laser focus. To address these issues, gas flow systems for spatter and fume removal have been commonly implemented. In this study, the object is improving clear rate of spatter and fume in a PBF chamber using gas flow. For evaluating the influence of inert gas flow on the behavior of spatter and fume, a solid-gas multiphase flow analysis was conducted. In addition, experimental observations of spatter behavior were conducted with a digital camera to validate the simulation results. As a result, the simulation showed that increasing the gas flow rate could enhance the clear rate of spatter and fume. And improved model had a higher clear rate than the conventional model. The experiments showed that considering the laser irradiation position and the scanning direction should be taken into account in the simulation.*

1 INTRODUCTION

There are numerous types of metal products, which have a huge impact on our lives [1]. In metal processing, engineers and researchers aim to decrease lead time and cost while maintaining accuracy. Industries have focused on subtractive and forming processes such as machining, grinding and casting, since these processes can easily ensure the accuracy and productivity through innovations in measurement systems [2]. However, subtractive and forming processes have some disadvantages. For example, the fabrication of complex-shaped products often requires the assembly of multiple components. These processes involve significant material waste due to their material removal characteristics. In contrast to subtractive and forming processes, additive manufacturing (AM) can fabricate complex-shaped parts in a layer-by-layer manner. This technology enables the fabrication of complex-shaped products in a single process while minimizing material usage. Some AM techniques also allow material recycling after fabrication. Therefore, AM has been attracting attention as a new manufacturing

technology [3]. Powder bed fusion (PBF) is one of the AM techniques in which powder layers are successfully spread, selectively melted and solidified with a laser beam. This process is usually performed in an inert gas atmosphere to prevent oxidation. This technique enables the fabrication of metal parts with higher precision and density than those produced by other AM techniques [4, 5]. Due to these advantages, this technique has been adopted in various industries, such as aviation, space and automotive. With the laser irradiation to the metal powder, powder temperature exceeds the evaporation point, generating metallic vapor. This remains inside the build chamber. This floating metal vapor (fume) causes laser attenuation and shifts the laser focus [6, 7, 8]. The fume also entrains and disperses the powder particles around the melt pool. Simultaneously, molten pool is ejected due to evaporation and Marangoni effects and subsequently cools and solidifies into particles. These particles, referred to as spatter, adhere to the surface of fabricated parts and decrease mechanical properties such as strength and elongation [2,7,9]. In recent years, blowing inert gas has become a common method to remove spatter and fume, because the particle size distribution (PSD) of spatter is from 10 to 120 μm, and the PSD of fume is from 0.1 to 2 μm [7,10]. I. Bitharas et al. investigated the interaction between spatter and inert gas flow and visualized the motion of spatter and fume using a high-magnification schlieren system. This result indicates that increasing the inert gas flow velocity led to a reduction in the amount of spatters [8]. Xiaobing et al. analyzed the motion of spatter in the build chamber using a fully coupled computational fluid dynamics (CFD) and discrete phase model (DPM). Spatter clear rate was calculated by varying the gas flow rate. Those results indicate that an increased gas flow rate led to a higher spatter clear rate. The clear rate reached 93% with an improved build chamber model [6]. Johaness et al. developed a numerical model including thermal effect and conducted transient simulations. The number of spatters deposited on the substrate changed with the gas flow rate. In addition, convective flow induced by intense heat influx through the melt pool was found to play a significant role in particle deposition in the substrate region. These results suggest that transient and compressible flow effects should be taken account in numerical modeling [11]. Yongqiang et al. tried to fabricate large-scale parts and investigated the interaction between gas flow and part quality using simulations and experiments. The gas flow velocity varied depending on the position within the fabrication area (powder bed). Inconsistency in the gas flow direction on the powder bed caused spatter redeposition and reduced tensile properties. In addition, keeping a gas flow parallel to the powder bed was found to be crucial for improving part quality consistency during large-scale PBF [12]. Based on these studies, improvement of the gas flow system has a huge impact on spatter generation and the clear rate which can reach over 90%. Nevertheless, validation of numerical simulations remains essential because PBF involves complex multiphysics interactions. Therefore, the objective of this study was to develop a gas flow system that provides consistent and parallel gas flow across the entire powder bed. A high clear rate (CR) and a high complete clear rate (CCR) were pursued varying the gas flow rate and geometry of the gas flow system. Both CFD and DPM simulation were conducted to validate the results.

2 PHYSICAL AND NUMERICAL MODEL

2.1 Modeling strategy

The PBF fabrication process involves numerous physical phenomena, such as fluid dynamics and thermodynamics. In addition, appropriate physical models should be selected depending on the scales of interest (e.g., part scale, meso-scale or micro scale), because the dominant physical phenomena differ at each scale and the computational resources are limited.

Chamber scale was selected in this study. A 3D-CAD model for the simulation and a schematic diagram of modeling are shown in Figure 1. The designed 3D-CAD model of the build chamber, corresponding to that a PBF machine, was created for numerical simulation. Ansys Fluent 2024 R1 was employed to simulate gas flow from the inlet to the outlet, while spatter and fume were generated at specific angles and velocities, resulting in their deposition on bottom of the build chamber or discharge through the outlet. The gas flow influenced the motion of spatter and fume, and the motion of spatter and fume influenced the gas flow. This configuration enabled easy adjustment of geometry of gas flow system and the gas flow rate, facilitating the identification of appropriate gas flow.

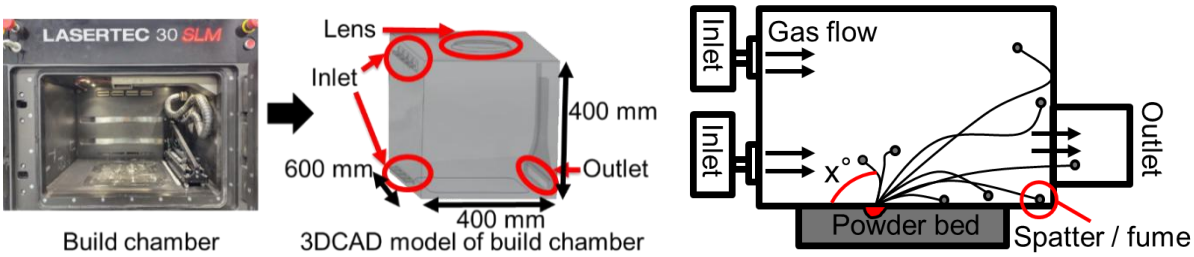

(a) 3D-CAD model of the build chamber (b) Schematic diagram of modeling

Figure 1: Simulation setup

2.2 Governing equations

Ansys Fluent 2024 R1 was employed to analyze the motion of gas flow, spatter and fume, because this software can simulate both compressible and incompressible fluids, as well as turbulent and laminar flows. Euler-Euler model equations and Euler-Lagrange model equations are two major approaches used to calculate the motion of multiphase flow. In this study, the latter approach was adopted, in which the fluid was treated as the continuous phase and particles were treated as the discrete phase. This model equation allowed consideration of the motion of each individual particle.

First, the motion of the gas flow can be expressed as [13]:

$$\nabla \cdot (\rho \vec{u}) = 0 \tag{1}$$

$$\frac{\partial}{\partial t}(\rho \vec{u}) + \nabla \cdot (\rho \vec{u}\vec{u}) = -\nabla p + \nabla \cdot (\bar{\bar{\tau}}) + \rho \vec{g} + \vec{F} \tag{2}$$

where ρ is the fluid density, $\vec{u}$ is the fluid velocity, p is the pressure, $\bar{\bar{\tau}}$ is the stress tensor, $\vec{g}$ is the gravitational acceleration and $\vec{F}$ is the external volumetric force. Solving Equation (1) and (2), which are simultaneous second-order partial differential equations, is difficult. In this study, Reynolds-averaged Navier-Stokes equations were used, assuming that the turblence intensity was in a steady state over a long time scale. The scalar amount (φ), such as pressure, is expressed as:

$$\varphi = \bar{\varphi} + \varphi' \tag{3}$$

where $\bar{\varphi}$ is the mean (time-averaged) component and the φ' is the fluctuating component. The time averaged equations are expressed as:

$$\frac{\partial}{\partial x_i}(\rho \bar{u_i}) = 0 \tag{4}$$

$$\frac{\partial}{\partial t}(\rho\overline{u_\iota}) + \frac{\partial}{\partial x_j}\left(\rho\overline{u_\iota}\,\overline{u_j}\right) = -\frac{\partial p}{\partial x_i} + \mu\frac{\partial}{\partial x_j}\left(\frac{\partial \overline{u_\iota}}{\partial x_j} + \frac{\partial \overline{u_j}}{\partial x_i} - \frac{2}{3}\delta_{ij}\frac{\partial \overline{u_l}}{\partial x_l}\right) + \frac{\partial}{\partial x_j}(-\rho\overline{u_i' u_j'}) \tag{5}$$

where $\overline{u_\iota}$ is the mean fluid velocity, μ is the fluid viscosity and u_i' is the fluctuating fluid velocity. In Equation (5), the term $-\rho\overline{u_i' u_j'}$ represents the effects of turbulence, which are modeled using k-ε model. The effect of turbulence can be expressed as:

$$-\rho\overline{u_i' u_j'} = \mu_t\left(\frac{\partial u_i}{\partial x_j} + \frac{\partial u_j}{\partial x_i}\right) - \frac{2}{3}\left(\rho k + \mu_t\frac{\partial u_l}{\partial x_l}\right)\delta_{ij} \tag{6}$$

where μ_t is the eddy viscosity and k is the turbulence kinetic energy. The μ_t is expressed as:

$$\mu_t = C_\mu \rho\frac{k^2}{\varepsilon} \tag{7}$$

where C_μ is the model constant and ε is the turbulence eddy dissipation.

Second, the motion of spatter and fume can be expressed as:

$$\frac{d\overrightarrow{u_p}}{dt} = \frac{\vec{u} - \overrightarrow{u_p}}{\tau_r} + \frac{\vec{g}\left(\rho_p - \rho\right)}{\rho_p} + \overrightarrow{F'} \tag{8}$$

where $\overrightarrow{u_p}$ is the particle velocity, τ_r is the particle relaxation time, ρ_p is the particle density and $\vec{F}'$ is the additional acceleration. The particle relaxation time (τ_r) is expressed as:

$$\tau_r = \frac{\rho_p {d_p}^2}{18\mu}\frac{24}{C_d Re} \tag{9}$$

where d_p is the particle diameter, C_d is the drag coefficient and Re is the relative Reynolds number. In addition, the effects of Saffman lift force is introduced to analyze the motion of fume because the fume diameter is often smaller than 1 μm. The Saffman lift force among $\overrightarrow{F'}$ in the Equation (8) is given as:

$$\overrightarrow{F'} = \frac{2Kv^{\frac{1}{2}}\rho d_{ij}}{\rho_p d_p (d_{lk}d_{kl})^{\frac{1}{4}}}\left(\vec{u} - \overrightarrow{u_p}\right) \tag{10}$$

where K is the coefficient for Saffman lift force, v is the kinematic fluid viscosity and d_{ij} is the deformation gradient tensor. In the case of analyzing the motion of fume, τ_r is given as:

$$\tau_r = \frac{\rho_p {d_p}^2 C_c}{18\mu}\frac{24}{C_d Re} \tag{11}$$

where C_c is the Cunningham correction factor.

2.3 Gas flow, spatter and fume initial conditions and parameters

According to previous studies, extensive experimental data are available on the diameters and ejection behavior of spatter and fume. In this study, particle size distributions (PSDs) were

defined, as shown in Figure 2. These PSDs follow the Rosin-Rammler distribution. The details of analysis conditions and physical properties are shown in Tables 1 and 2 [6, 7]. Simulation results were obtained by varying the gas flow rate from 500 L/min to 3000 L/min.

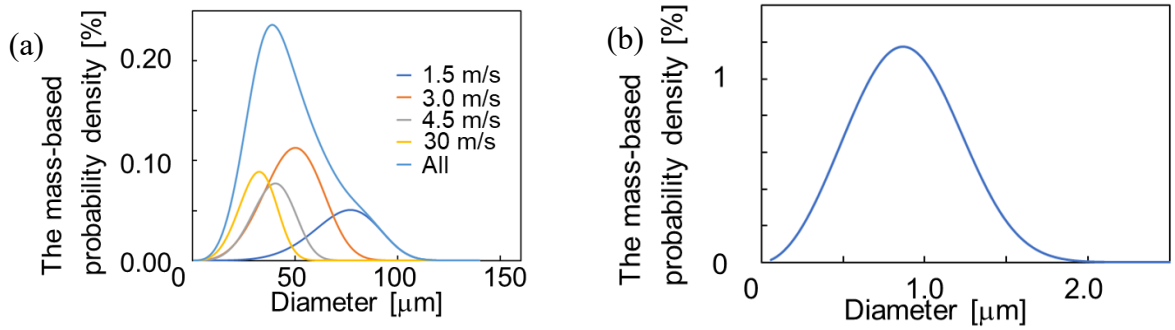

Figure 2: The PSDs of (a) spatter and (b) fume

Table 1: Analysis conditions

Inert gas	Argon
Gas flow rate [L/min]	500 – 3000
Powder	SUS316L
Shape	Sphere
Shear condition of walls	No slip
Spatter and fume ejection velocity [m/s]	1.5 – 35
Spatter and fume ejection direction [°]	30 - 150

Table 2: Physical properties

	Density [kg/m^3]	Viscosity [kg/m s]
Fluid (Argon)	1.784	2.223×10^{-5}
Powder (SUS316L)	7980	-
Wall (Aluminum)	2710	-

Spatters deposited on the powder bed degrade the quality of the fabricated parts, as shown in Figure 3(a). In addition, when spatters adhere to the lens, the adhered spatters can be burned by laser irradiation, which may result in lens damage, as shown in Figure 3(b). In this study, spatters deposited on the bottom of the build chamber or adhered to the lens were defined as trapped spatters for counting purposes, as shown in Figure 3(c). Even when spatters deposit outside the powder bed, they can return to the powder bed and mix with fresh powders due to the motion of the recoating blade. For these reasons, spatters should be discharged through the outlet. Furthermore, the discharged spatters are collected and recycled as material. Spatters that reach the outlet were also defined as trapped spatters, as shown in Figure 3(c). The clear rate (CR) and the complete clear rate (CCR) were defined as:

$$Clear\ rate\ (CR) = 100 \times \frac{n_{outside\ powder\ bed} + n_{lens} + n_{discharged}}{N} \tag{12}$$

$$Complete\ clear\ rate\ (CCR) = 100 \times \frac{n_{\ discharged}}{N} \tag{13}$$

where $n_{outside\ powder\ bed}$ is the number of spatters that deposit outside the powder bed, n_{lens} is the number of spatters that adhere to the lens, $n_{discharged}$ is the number of spatter discharged thorough the outlet and N is the total number of generated spatters. These values enabled evaluation of the effects of spatter behavior.

In this study, spatters were configured to be generated and ejected in the y-direction from the powder bed for simplicity, considering the most severe condition in which spatters were ejected toward the inlet side. The generation points were uniformly located on the powder bed, as shown in Figure 3(d).

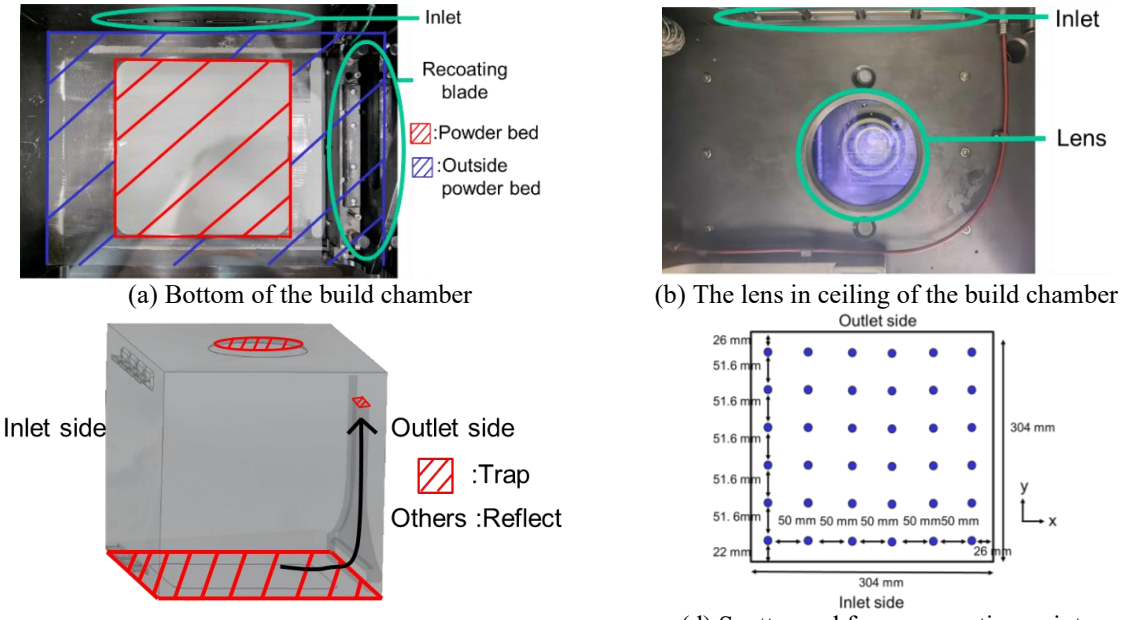

(a) Bottom of the build chamber

(b) The lens in ceiling of the build chamber

(c) The definition of walls

(d) Spatter and fume generation points on the powder bed

Figure 3: DPM setup

2.4 Model validation

The initial ejection angle of spatter influences the trajectories and removal behavior [6, 14]. Furthermore, spatter removal process involves several physical phenomena, which reduce the validity of simulation results. Videos of spatter trajectories were recorded using a camera due to confirm the validity of simulation results. Table 3 provides the fabrication conditions used in the experiments. The gas flow velocity, the scanning direction and the observation position were varied during the experiments. The scanning direction is shown in Figure 4(a) and the observation position and the fabricated parts are shown in Figure 4(b). Blocks measuring 10 mm × 10 mm × 1.05 mm were fabricated on the base plate measuring 304 mm × 304 mm × 20 mm using a powder bed fusion machine (LASERTEC 30 SLM 1st Generation, DMG Mori Co., Ltd.). In this study, three parameters were calculated from each frame due to determine the initial ejection angle and velocity, and to evaluate the effect of gas flow rate on the spatter trajectory, as shown in Figure 4(c). The initial ejection angle of spatter was denoted as ∠AOC, the trajectory angle of spatter as ∠BAC', and initial ejection velocity of spatter in the yz plane (v) was expressed as:

$$v = \sqrt{(y2 - y1)^2 + (z2 - z1)^2} \times 120 \tag{14}$$

Table 3: Fabrication conditions

Powder	SUS316L
Spot diameter [μm]	80
Track width [mm]	0.7
Scanning velocity [mm/s]	600
Laser power [W]	201
Gas flow rate [L/min]	300 – 500
Object height for video capture [mm]	0.05 – 0.20

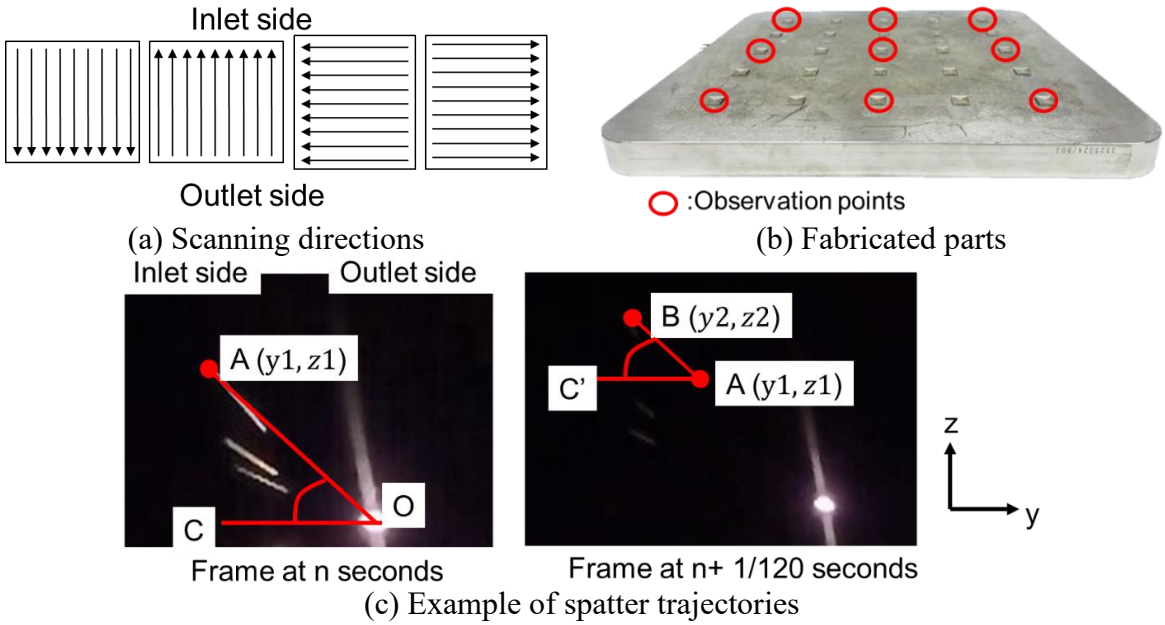

Figure 4: Experimental setup

3 RESULTS AND DISCUSSION

3.1 Numerical results

3.1.1 Numerical results for conventional gas flow system

To clarify the current condition of the gas flow system, the velocity distribution as well as the CR and CCR were analyzed. Figure 5(a) provides the gas flow velocity distribution at 30 mm above the bottom of the build chamber, and Figure 5(b) shows the distribution at the center of the build chamber. Increasing the gas flow rate led to the higher gas flow velocity; however, the gas flow velocity was uneven across the entire powder bed. This unevenness reduced the CR and CCR in regions where the gas flow velocity was low. As observed by other researchers, the Coanda effect directs the gas flow towards the powder bed [6, 12]. Figure 6 shows the spatter and fume trajectories. The gas flow rate influenced the spatter and fume trajectories because higher velocity generated larger drag forces, resulting in farther transportation. Since fumes are lighter and smaller Stokes number than spatters, they tend to follow the gas flow more closely. The CR and CCR of spatter and fume are shown in Figure 7. Increasing the gas flow rate improved the CR and CCR of spatter, as higher drag forces transported spatters farther. The maximum CR of spatter was 78.4%, although the maximum CCR of spatter was 33.3%.

Regions of low gas velocity area, the Coanda effect, and small outlet size may have prevented spatters from being discharged effectively. In contrast, the gas flow rate had little influence on the CR and CCR of fume; the maximum CCR was 55.3%. Circulating flow within the build chamber may have been responsible for the persistence of floating fumes.

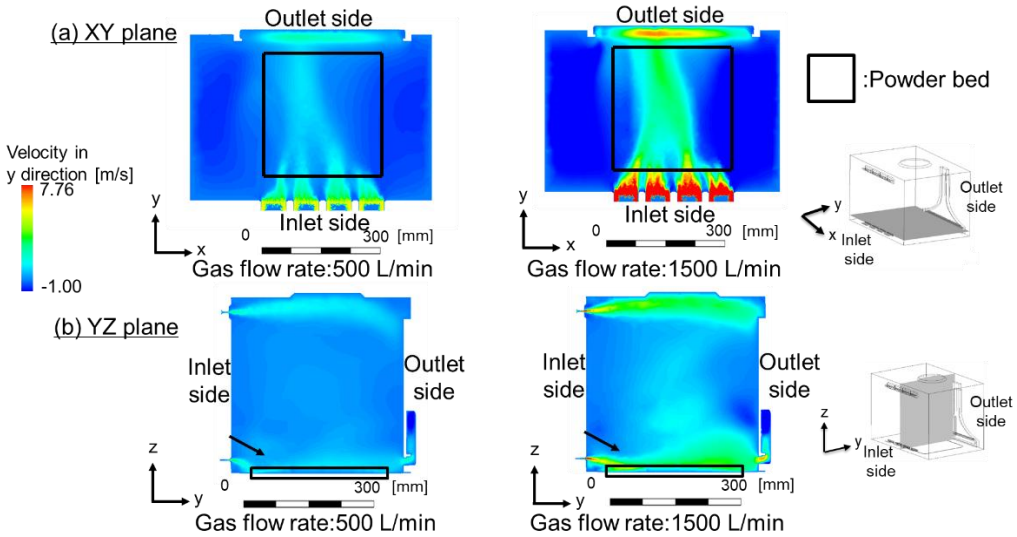

Figure 5: The gas flow velocity distribution at (a) XY and (b) YZ plane of the conventional model

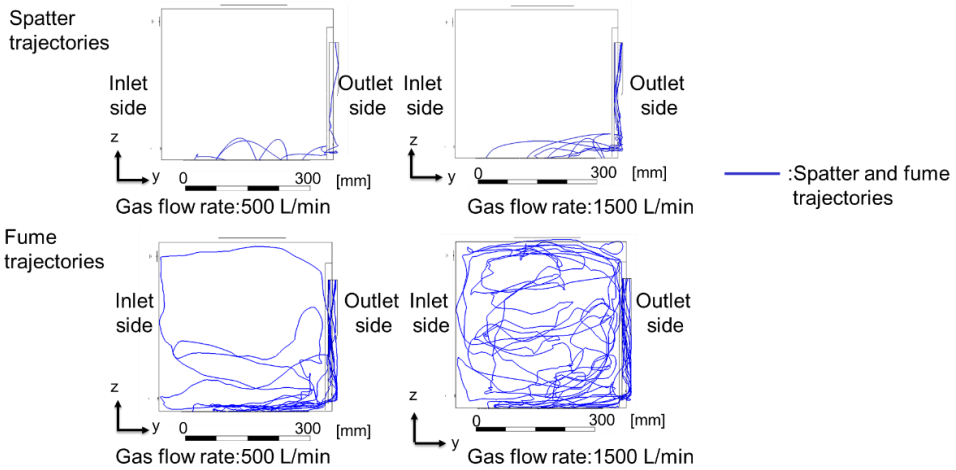

Figure 6: Spatter and fume trajectories of the conventional model

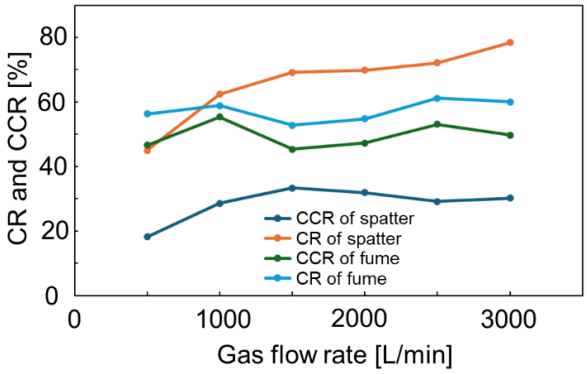

Figure 7: The CR and CCR of the conventional model

3.1.2 Numerical results for improved gas flow system

An improved 3D-CAD model of the build chamber was developed through geometric modifications. In this model, a single large inlet replaced the original eight inlets, and the inlet and outlet geometries were made identical. These modifications were intended to promote a more uniform gas flow that transports spatter and fume directly from the inlet to the outlet, similar to flow through a tunnel, as shown in Figure 8. Furthermore, the inlet and outlet positions were lowered to minimize the Coanda effect. Three different inlet and outlet heights were considered.

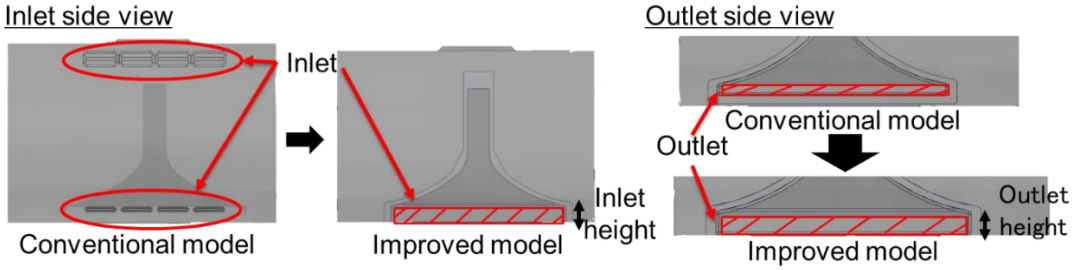

Figure 8: The 3D-CAD model of the improved build chamber

In contrast to the conventional model, the gas flow covered wider area across the powder bed, as shown in Figure 9(a). In addition, the flow direction was more upward, as shown in Figure 9(b). These results indicate that the improved model effectively suppresses the Coanda effect. The spatter and fume trajectories are presented in Figure 10. The fume circulated less than in a conventional model and was more likely to follow the gas flow. Figure 11 provides the CR and CCR of spatter and fume in the improved model. Based on these improvements, the CR and CCR of the improved model were higher than those of the conventional model. The maximum CCR of spatter increased from 22.9% to 64.3%.

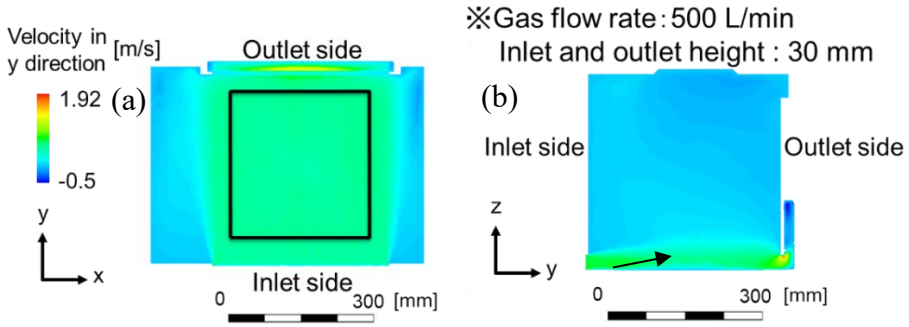

Figure 9: The gas flow velocity distributions at (a) XY and (b) YZ plane of the improved model

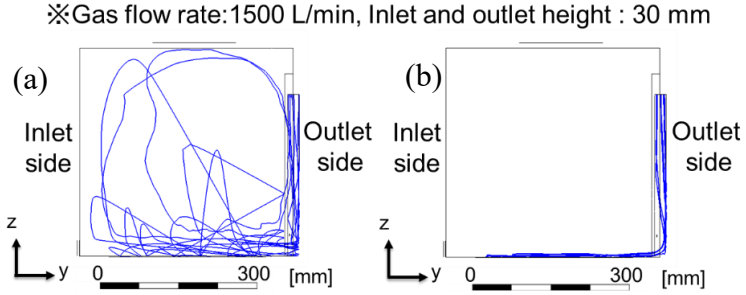

Figure 10: (a) Spatter and (b) fume trajectories of the improved model

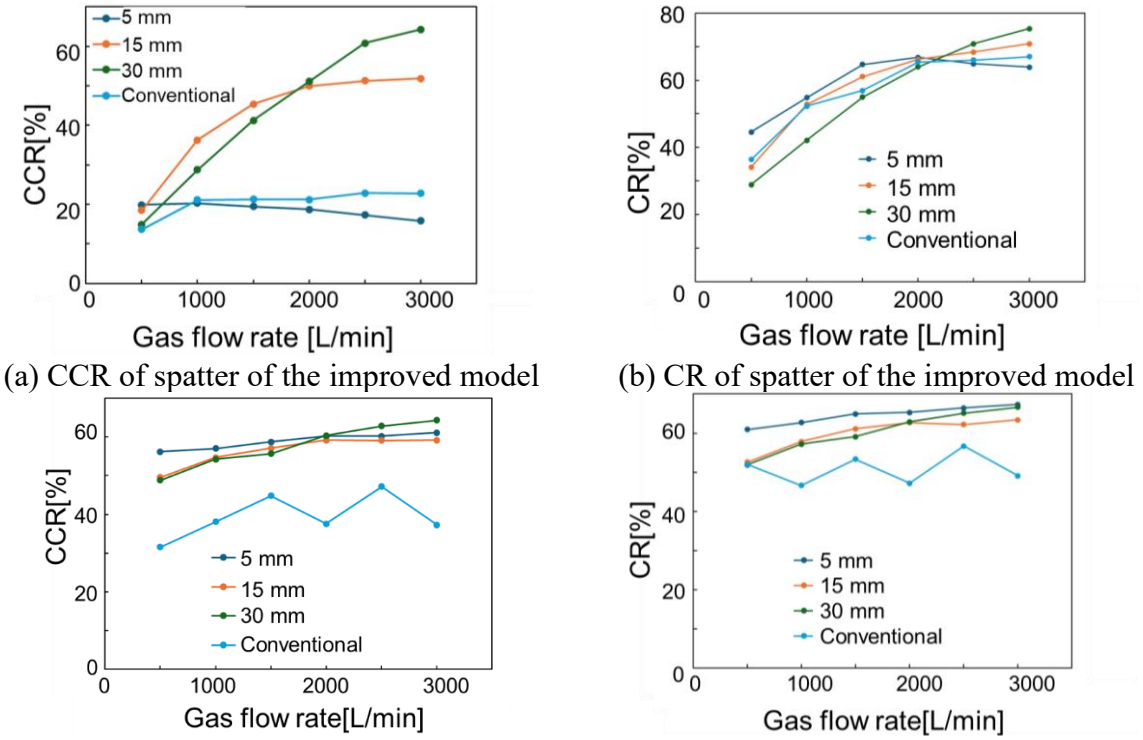

(a) CCR of spatter of the improved model (b) CR of spatter of the improved model

(c) CCR of fume of the improved model (d) CR of fume of the improved model

Figure 11: The CR and CCR of spatter and fume in an improved model

3.2 Model validation

The trajectories of spatter captured using camera provided ejection velocity-direction and trajectory velocity-direction distributions. The ejection velocity-direction distributions indicate the interaction between the initial ejection angle and velocity, whereas the trajectory velocity-direction distributions indicate the interaction between spatter trajectories and ejection velocity, including the effects of gas flow. Depending on the position of the laser irradiation, the initial ejection angles differed, as shown in Figure 12. The variation in laser irradiation angles may have induced different molten pool geometries, influencing the mechanism of spatter generation. Furthermore, higher gas flow velocity could cool the molten pool more rapidly and may have prevented the formation of droplet spatters, because spatters tended to eject vertically in regions of higher gas flow velocity [15]. Depending on the scanning direction, the initial ejection angles of spatters also varied, and spatters were more likely to eject opposite to the scanning direction, as shown in Figure 13. Figure 14 shows the trajectory velocity-direction distribution of spatters. When the scanning and gas flow directions were the same, spatters tended to eject opposite to the gas flow. When the scanning and gas flow directions were opposite, spatters were more likely to eject in the same direction as the gas flow. In addition, an increase in gas flow rate led to horizontal spatter ejection. According to these results, the gas flow influenced the spatter trajectories; however, the initial ejection angle had a dominant effect. The differences of the spatter ejection angle and velocity depending on the irradiation position and scanning direction should be taken account into the simulation.

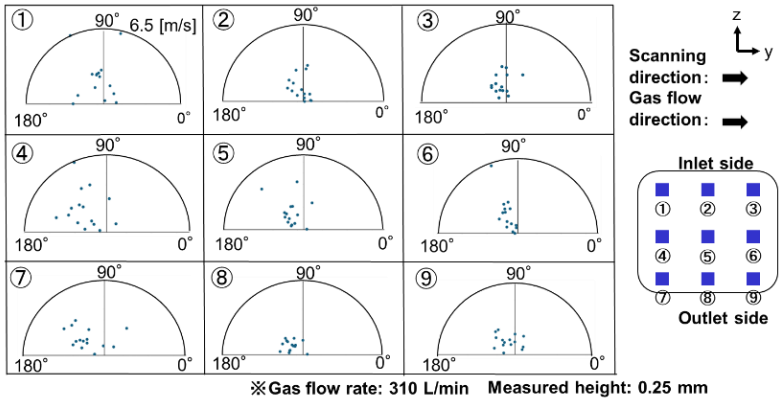

Figure 12: The ejection velocity-direction distributions of spatter in which the laser irradiation position is varied

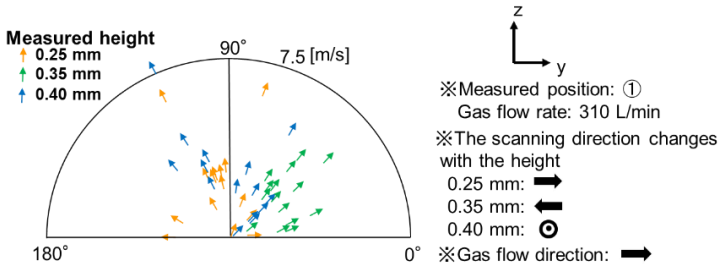

Figure 13: The ejection velocity-direction distribution of spatter in which the scanning direction is varied

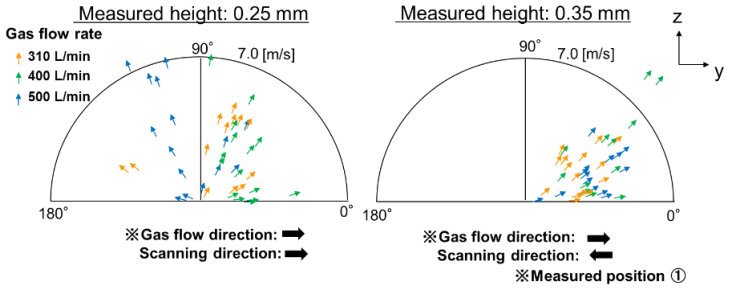

Figure 14: The trajectory velocity-direction distributions of spatter in which the gas flow rate is varied

4 CONCLUSIONS

In this study, the spatter and fume trajectories were obtained using the coupled CFD-DPM model, and the experimental results validated the simulation results. The key findings are summarized as follows:

- Depending on the gas flow rate, the gas flow velocity and the spatter and fume trajectories differed. The maximum CCR of spatter increased from 22.9% to 64.3% in the improved model.
- The spatter initial ejection angles and velocities are different depending on the positions of the laser irradiation and scanning direction.

REFERENCES

[1] S. Melcote, S. Liang, T. Özel, I. S. Jawahir, D. A. Stephenson, B. Wang, (2022). A Review of Advances in Modeling of Conventional Machining Processes: From Merchant to the Present. *Article in Journal of Manufacturing Science and Engineering,* vol. 144 (11),

110801. https://doi.org/10.1115/1.4053522

[2] C. Kato, T. Ikeshoji, M. Yonehara, S. Akiyama, I. Murakami, Y. Hashizume, H. Kyogoku, (2020). Influence of powder particle morphology on properties of Al-10Si-0.4Mg alloy fabricated by high-power and high-speed conditions of laser powder bed fusion process. *Journal of The Japan Institute of Light Metals*. vol. 70 (10), 475-482. https://doi.org/10.2464/jilm.70.475

[3] H. Kyogoku, (2014). Research Trend and Application of Additive Manufacturing. *Journal of smart processing*. vol. 3 (3), 148-151. https://doi.org/10.7791/jspmee.3.148

[4] H. Kyogoku, T. Ikeshoji, (2020). A review of metal additive manufacturing technologies: Mechanism of defects formation and simulation of melting and solidification phenomena in laser powder bed fusion process. *Mechanical Engineering Reviews*. vol. 7 (1), 19-00182. https://doi.org/10.1299/mer.19-00182

[5] M. Yamaguchi, K. Kushima, Y. Ono, T. Sugai, T. Oyama, T. Furumoto, (2023). Humidity control in laser powder bed fusion using titanium alloy powder for quality assurance of built parts and reusability of metal powder. *Journal of Materials Processing Technology*. vol. 311, 117817. https://doi.org/10.1016/j.jmatprotec.2022.117817

[6] X. Zhang, B. Cheng, C. Tuffile, (2020). Simulation study of the spatter removal process and optimization design of gas flow system in laser powder bed fusion. *Additive Manufacturing*. vol. 32, 101049. https://doi.org/10.1016/j.addma.2020.101049

[7] Y. Miyazaki, S. Katayama, (2013). Influence of laser-induced plume on penetration in laser welding. *Quarterly journal of the Japan Welding Society*. vol. 31 (2), 119-125. https://doi.org/10.2207/qjjws.31.119

[8] I. Bitharas, A. Burton, A.J. Ross, A.J. Moore, (2021). Visualisation and numerical analysis of laser powder bed fusion under cross-flow. *Additive Manufacturing*. vol. 37, 101690. https://doi.org/10.1016/j.addma.2020.101690

[9] I. Koutiri, E. Pessardb, P. Peyrea, O. Amloua, T. D. Terrisa, (2018). Influence of SLM process parameters on the surface finish, porosity rate and fatigue behavior of as-built Inconel 625 parts. *Journal of Materials Processing Technology*. vol. 255, 536-546. https://doi.org/10.1016/j.jmatprotec.2017.12.043

[10] J. Takahashi, H. Nakashima, N. Fujii, (2020). Fume particle size distribution and fume generation rate during arc welding of cast iron. *Industrial Health*. vol. 58 (4), 325-334. https://doi.org/10.2486/indhealth.2019-0161

[11] C. Johannes Altmepppen, Robert Nekic, Philipp Wagenblast, Stephan Staudacher, (2021). Transient simulation of particle transport and deposition in the laser powder bed fusion process: A new approach to model particle and heat ejection from the melt pool. *Additive manufacturing*. vol. 46, 102135. https://doi.org/10.1016/j.addma.2021.102135

[12] Y. Yang, Z. Chen, Z. Liu, H. Wang, Y. Zhang, D. Wang, (2023). Influence of shielding gas flow consistency on parts quality consistency during large-scale laser powder bed fusion. *Optics and Laser Technology*. vol. 158 (Part A), 108899. https://doi.org/10.1016/j.optlastec.2022.108899

[13] Ansys, Inc., (2024). Ansys fluent theory guide.

[14] A.B.S. Alquaity, (2025). Influence of nozzle diameter and gas flow on spatter removal in laser powder bed fusion: A CFD approach. *Results in Engineering*. vol. 25, 103759. https://doi.org/10.2486/indhealth.2019-0161

[15] D. Wang, S. Wu, F. Fu, S. Mai, Y. Yang, Y. Liub, C. Song, (2017). Mechanisms and characteristics of spatter generation in SLM processing and its effect on the properties. *Material and Design*. vol. 117, 121-130. https://doi.org/10.1016/j.matdes.2016.12.060